POLITECNICO DI TORINO
Repository ISTITUZIONALE

Low-Velocity Impact in Composite Plates Using the Hashin 3D Criterion and 2D Layer-Wise Theories

Original
Low-Velocity Impact in Composite Plates Using the Hashin 3D Criterion and 2D Layer-Wise Theories / Petrolo, M., Filippi, M., Carrera, E., Franceschini, C., Tortorelli, E.. - In: AEROTECNICA MISSILI & SPAZIO. - ISSN 2524-6968. - ELETTRONICO. - 105:6(2026), pp. 923-936. [10.1007/s42496-026-00320-9]

Availability:
This version is available at: 11583/3016268 since: 2026-10-03T13:51:39Z

Publisher:
Springer

Published
DOI:10.1007/s42496-026-00320-9

Terms of use:

This article is made available under terms and conditions as specified in the corresponding bibliographic description in the repository

Publisher copyright

(Article begins on next page)

26 November 2026

Aerotecnica Missili & Spazio (2026) 105:923–936
https://doi.org/10.1007/s42496-026-00320-9

RESEARCH

Low-velocity Impact in Composite Plates Using the Hashin 3D Criterion and 2D Layer-Wise Theories

M. Petrolo[1] · M. Filippi[1] · E. Carrera[1] · C. Franceschini[1] · E. Tortorelli[1]

Received: 24 February 2026 / Revised: 27 April 2026 / Accepted: 27 May 2026 / Published online: 3 July 2026
© The Author(s) 2026

Abstract
The present work investigates the low-velocity impact response of composite laminate plates using the Carrera Unified Formulation for structural modelling, the 3D Hashin failure criterion for damage evaluation, and cohesive elements. 2D structural theories are employed, based on a layer-wise approach, capable of accurate modeling of transverse stresses and delamination. The numerical examples consider three cases, and the results are verified and validated with numerical models and experiments retrieved from the literature. The results show the advantages of the present formulation in reducing computational costs compared to 3D finite elements; the need for parabolic displacement fields within each layer for good accuracy; improvements in the oscillatory behavior of the time response; and the proper detection of damage distributions over the 3D domain.

Keywords Carrera Unified Formulation (CUF) · Low-velocity impact · Higher-order structural modeling · Continuum damage mechanics · Delamination

1 Introduction

Carbon Fiber Reinforced Polymer (CFRP) composites offer significant advantages in aeronautical applications, thanks to their high strength-to-weight ratio [1]. In both civil and military aircraft, various fibers have been used, but the most common is carbon fiber. Key concerns in adopting composite materials include impact resistance and damage tolerance. Impact response is one of the most critical loading cases for the lightweight, layered structures widely used in aerospace. In particular, low-velocity impact (LVI) is a localized event that can introduce intralaminar and interlaminar damage that is difficult to detect visually. As a consequence, the residual strength of the structure is reduced. CFRP does not exhibit extensive plastic deformation. Beyond the elastic regime, their response is often nonlinear, primarily due to progressive damage mechanisms such as matrix cracking, fibre fracture, and interlaminar delamination. This paper focuses on low-velocity impacts; the reference velocity range is on the order of a few m/s, even if there is no clear transition between low and high velocity [2].

Given the variability of impact scenarios across location, boundary conditions, and contact dynamics, predictive capabilities are essential to avoid extensive experimental testing [3, 4]. Moreover, numerical simulation helps reduce costly testing and enables rapid sensitivity studies to optimize the design [5, 6]. This, in turn, allows prediction of damage scenarios and stiffness degradation over time [7, 8]. Simplified analytical approaches have been developed [9]. While computationally efficient, they provide only global predictions and cannot capture localized damage mechanisms. Computational approaches for damage simulation are generally divided into two main categories. Discrete damage models, such as those based on cohesive zone methods (CZM) [10], provide detailed damage representation

✉ M. Petrolo
marco.petrolo@polito.it

M. Filippi
matteo.filippi@polito.it

E. Carrera
erasmo.carrera@polito.it

C. Franceschini
chiara.franceschini@polito.it

E. Tortorelli
elisa.tortorelli@polito.it

[1] MUL² Lab, Department of Mechanical and Aerospace Engineering, Politecnico di Torino, Corso Duca degli Abruzzi 24, 10129 Torino, Italy

but are often computationally demanding. As an alternative, continuum damage mechanics (CDM) [11] enables efficient damage simulation with reduced numerical overhead. The literature on modelling impact damage in laminated composites is extensive [9]. However, it is widely recognized that relying on a single damage modelling paradigm, either CZM or CDM alone, is not recommended to capture the overall response [2]. Advanced finite element (FE) formulations have incorporated continuous damage mechanics with interface-based delamination models, significantly improving predictive capabilities. Nonetheless, these methods still require careful selection of the damage initiation criterion, the evolution law, and the material parameters [12].

This work follows the methodology proposed by Nagaraj [13, 14] and is based on the Carrera Unified Formulation (CUF). The focus is on the use of higher-order 2D structural theories with layer-wise (LW) capabilities, capable of obtaining the 3D stress field necessary for accurate predictions of failure onset and propagation. The present paper introduces a different intralaminar failure assessment, i.e., rather than using the CODAM2 approach [11], a 3D Hashin criterion is employed [15–17]. Delamination is modelled via cohesive interface elements [10, 18, 19] with linear damage evolution.

This work is structured as follows: Sect. 2 presents the structural theories and the FE formulation adopted. Section 3 presents damage models and contact. Numerical results for the three case studies are reported in Sect. 4, and the main conclusions are drawn in Sect. 5.

2 Structural Theories and FE Formulation

The structural theories adopted in this paper are based on the Carrera Unified Formulation [20], which employs higher-order Lagrange polynomial expansions and yields an LW representation through the laminate thickness. CUF enables the use of higher-order 1D and 2D theories thanks to a compact notation: the displacement fields, over the cross-section for beams and through the thickness for plates and shells, are modeled using expansion functions whose type and order are arbitrary.

The 3D displacements of the *k*-th ply of the laminated plate, considering a LW modeling approach for a 2D theory, can be expressed as:

$$\boldsymbol{u}^k(x, y, \zeta_k) = F_\tau^k(\zeta_k)\, \boldsymbol{u}_\tau^k(x, y), \qquad \tau = 1, \ldots, M \tag{1}$$

where $F_\tau(\zeta_k)$ of M terms describes the kinematics through the local thickness domain $\zeta_k \in [-1, 1]$ and $\mathrm{u}_\tau^k(x, y)$ are the generalised displacement variables. The structural theory is chosen with F_τ. The present work employs Lagrange expansions of order *N*, denoted LE*N*, defined as:

$$F_\tau(\zeta_k) = \prod_{\substack{i=0 \\ i \neq s}}^{N} \frac{\zeta_k - \zeta_{ki}}{\zeta_{ks} - \zeta_{ki}}. \tag{2}$$

Here, ζ_{ks} are the interpolation points and $\zeta_{k0} = -1$ and $\zeta_{kN} = 1$ represent the bottom and top surfaces of the *k*-th ply. The LW approach provides accurate transverse stresses. Each layer has independent displacement variables, and continuity is imposed at the interface [21]. The FE discretization is handled using standard 9-node quadrilateral elements (Q9).

$$\boldsymbol{u}(x, y, z) = F_\tau(z) N_i(x, y) \boldsymbol{u}_{\tau i}, \quad \tau = 1, ..., M \quad i = 1, ..., p \tag{3}$$

The displacement field is given by the product of the nodal displacements $\boldsymbol{u}_{\tau i}$, the expansion functions F_τ(z) with *M* terms, and the 2D shape functions N_i(x,y), where *p* indicates the number of element nodes.

The 3D stress and strain components are:

$$\begin{aligned} \boldsymbol{\sigma} &= \{\sigma_{xx}, \sigma_{yy}, \sigma_{zz}, \sigma_{xy}, \sigma_{xz}, \sigma_{yz}\} \\ \boldsymbol{\epsilon} &= \{\epsilon_{xx}, \epsilon_{yy}, \epsilon_{zz}, \epsilon_{xy}, \epsilon_{xz}, \epsilon_{yz}\} \end{aligned} \tag{4}$$

The linear strain–displacement relation is:

$$\boldsymbol{\epsilon} = \mathbf{B}\boldsymbol{u} \tag{5}$$

where the linear differential operator is $\mathbf{B}$ [20]. The constitutive relation is written using $\mathbf{C}^{sec}$, the secant material stiffness matrix, including the damaged state.

$$\boldsymbol{\sigma} = \mathbf{C}^{\mathrm{sec}} \boldsymbol{\epsilon} \tag{6}$$

Explicit integration techniques are used [13], since implicit schemes may suffer from convergence issues. Once the lumped mass matrix $\mathbf{M}$ is evaluated, the acceleration is computed. The vectors $\mathbf{F}_{\mathrm{ext}}$ and $\mathbf{F}_{\mathrm{int}}$ are the external and internal force, respectively:

$$\ddot{\mathbf{u}}^{\,t+\Delta t} = \mathbf{M}^{-1} \left(\mathbf{F}_{\mathrm{ext}}^{t+\Delta t} - \mathbf{F}_{\mathrm{int}}^{t+\Delta t} \right) \tag{7}$$

The solution is calculated using the central difference scheme, the velocity within a time step is approximated at its mid-interval. This numerical approach is conditionally stable and it requires a time step Δt smaller than a critical threshold Δt_{crit}.

$$\Delta t \leq \Delta t_{\text{crit}} \approx \frac{2}{\omega_{\max}} \tag{8}$$

where $\omega_{\max}$ is the highest natural frequency and can be estimated through power-iteration techniques as:

$$\omega_{\max} = \sqrt{\lambda_{\max}} \tag{9}$$

where $\lambda_{\max}$ is the largest eigenvalue of the generalized eigenvalue problem.

3 Damage Model and Contact

In this section, intralaminar damage is addressed first, followed by interlaminar damage, and finally the contact formulation is presented.

3.1 Intralaminar Damage Model

The damage model [15, 16] comprises activation and progression of the damage. The 3D Hashin criterion, which accounts for failure in both fibers and matrix, predicts damage initiation under compression and tension. Here, the 3D Hashin model is adopted for fiber compression and matrix/fiber tension. For matrix compression, the Puck criterion [17] is considered. The fiber damage initiation occurs when failure index $\mathrm{F}_{ft} \geq 1$, with

$$F_{ft} = \left(\frac{\sigma_{11}}{X_T}\right)^2 + \alpha_f \left[\left(\frac{\sigma_{12}}{S_{12}}\right)^2 + \left(\frac{\sigma_{13}}{S_{13}}\right)^2\right] \tag{10}$$

X_T is the fiber tensile strength, and S_{12} and S_{13} are the shear strengths. α_f is the interaction coefficient for fibers and, unless otherwise stated, is set equal to zero. σ_{ij} are the stress components in the lamina material coordinate system, in particular σ_{11} is the normal stress in the fiber direction.

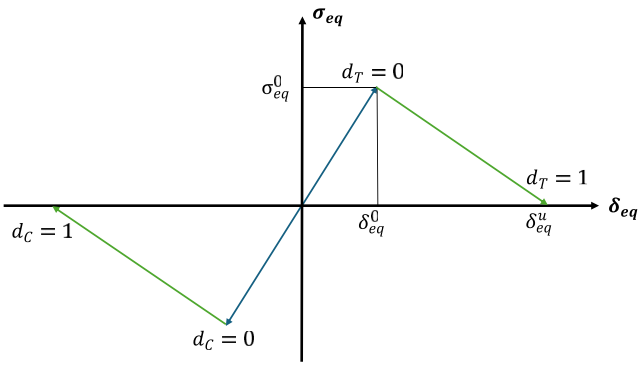


Fig. 1 Bilinear damage evolution

F_{mt} is the index for the matrix damage initiation along the transverse direction,

$$F_{mt} = \left(\frac{\sigma_{22}+\sigma_{33}}{Y_T}\right)^2 + \frac{1}{S_{23}^2}(\sigma_{23}^2 - \sigma_{22}\sigma_{33}) + \left(\frac{\sigma_{12}}{S_{12}}\right)^2 + \left(\frac{\sigma_{13}}{S_{13}}\right)^2 \tag{11}$$

Y_T is the matrix tensile strength, and S_{23} is the shear strength. Similarly, concerning compression, the failure index for the fiber is calculated as follows:

$$F_{fc} = \left(\frac{\sigma_{11}}{X_C}\right)^2 \tag{12}$$

where X_C is the fiber compressive strength. For matrix compression, the Puck criterion [17] is considered. The fracture of the matrix is due to σ_{nn}, σ_{nl}, σ_{nt}, which are, respectively, the normal to the fracture plane, longitudinal shear, and transverse shear stresses.

$$F_{mc} = \left(\frac{\sigma_{nt}}{S_{23}^A - \eta_{nt}\sigma_{nn}}\right)^2 + \left(\frac{\sigma_{nl}}{S_{13} - \eta_{nl}\sigma_{nn}}\right)^2 \tag{13}$$

η_{nt} and η_{nl} characterize the internal friction of the material based on the Mohr-Coulomb theory [22], while S_{23}^A is the transverse shear strength in the fracture plane. Once the failure criterion is triggered, damage progression follows a linear law, with the material stiffness decreasing until final failure. The four modes of damage use a unified subscript $P \in \{ft, fc, mt, mc\}$ and d_P is a parameter governing the evolution of damage in each mode,

$$d_P = \frac{\delta_{eq}^u(\delta_{eq} - \delta_{eq}^0)}{\delta_{eq}(\delta_{eq}^u - \delta_{eq}^0)} \tag{14}$$

$\delta_{eq}^0 = \delta_{eq}\big|_{F=1}$ is the equivalent displacement at the damage initiation, and, together with the equivalent stress, they are necessary to define the damage evolution. The damage progression criteria exploit equivalent tensile and compressive displacements δ_{eq}, for fibers and matrix; they are function of the characteristic length l_C, set equal to the cubic root of the Gauss point volume, $\mathrm{l}_C = (\mathrm{V}_{GP})^{1/3}$. Figure 1 shows the constitutive equivalent stress-displacement relation in which the ultimate displacement δ_{eq}^u corresponds to the damage saturation. The constitutive elastic stress–strain relation is modified in the damaged state,

$$\boldsymbol{\sigma} = \mathbf{C}_{dam}\boldsymbol{\epsilon} \tag{15}$$

$\mathbf{C}_{\text{dam}}$ is the stiffness matrix in the damage state, function of damage parameters d_P. More information about damage can be found in [15, 16].

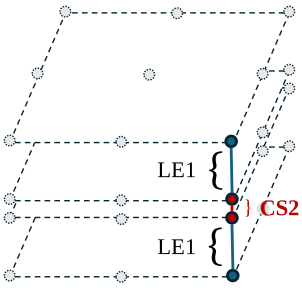


Fig. 2 Two-node cohesive Lagrange through thickness elements (CB2)

3.2 Interlaminar Damage Model

In the current 2D-CUF formulation, delamination is modeled using through-thickness cohesive interface elements placed between adjacent layer-wise structural expansions, as shown in Fig. 2. The three-dimensional displacement field is reconstructed through the standard CUF approximation, Eq. 1 and Eq. 3, while the displacement jump is modeled by the cohesive interface degrees of freedom and used in the traction–separation law. The mixed-mode cohesive law triggers delamination once a relative displacement threshold is exceeded [18, 19]. The following relation links the cohesive traction t_j to the displacement jump Δ_j in the local interface coordinate system, where Δ_3 denotes the normal component.

$$t_j = (1-d)\, D^0_{ij}\, \Delta_j \;-\; d\, D^0_{ij}\, \delta_{3j} \langle -\Delta_3 \rangle \tag{16}$$

$d \in [0,1]$ is the scalar damage variable, $\langle \cdot \rangle$ denotes the MacAuley bracket. D^0_{ij} is the initial stiffness tensor, penalty-based, dependent on the Kronecker delta δ_{ij} and on the penalty parameters K_n, K_s, and K_t, associated with the normal and the two tangential directions, respectively.

$$D^0_{ij} = K_i\, \delta_{ij}, \qquad K_1 = K_s,\; K_2 = K_t,\; K_3 = K_n \tag{17}$$

The mixed-mode propagation is inspired by the Benzeggagh–Kenane criterion,

$$G_c = G^c_I + (G^c_{II} - G^c_I)\,(G_T)^\eta \qquad G_T = \frac{G_{II}}{G_I + G_{II}}. \tag{18}$$

G_c is the critical mixed-mode energy release rate, while G_T is the mode-mixity ratio based on the energy release rates. The quantities G^c_I and G^c_{II} are the critical energy release rates in pure Mode I and pure Mode II, respectively, i.e., material fracture-toughness parameters. G_I and G_{II} are the current energy release rates calculated from the cohesive tractions and separations, used to quantify the relative contribution of each mode. This relation depends on η, an experimentally determined parameter set to 1.45 [19].

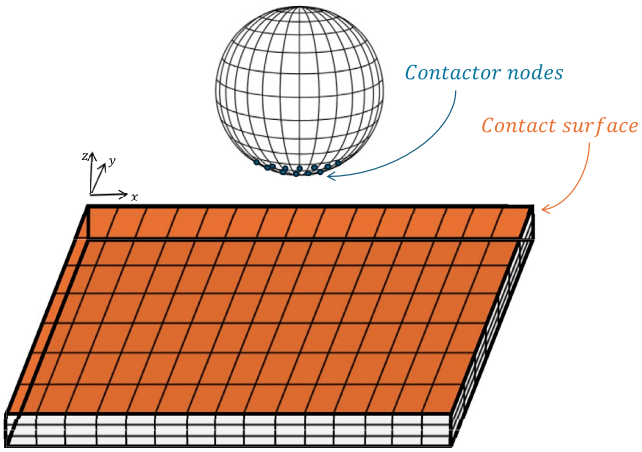


Fig. 3 Node-to-surface contact method

3.3 Contact

The present work adopts a node-to-surface approach and contact is enforced by constraining the contact node, in order to prevent the penetration of the target plate. Within the CUF framework, node-to-surface contact constraints can be enforced using Lagrange multiplier or penalty methods. Following the work of Carpenter [23], and within a central difference scheme, the forward-increment, time-shifted, coupling is written as

$$\mathbf{M}\,\ddot{\mathbf{u}}_n + \mathbf{F}_{\text{int}}(\mathbf{u}_n, \dot{\mathbf{u}}_n) + \mathbf{G}^{\mathrm{T}}_{n+1}\,\boldsymbol{\lambda}_n = \mathbf{F}_{\text{ext}}. \tag{19}$$

The incremental equation of motion is constrained by the no-penetration condition,

$$\mathbf{G}_{n+1}\,(\mathbf{u}_{n+1} + \mathbf{X}) = \mathbf{0} \tag{20}$$

$\mathbf{G}$ is the contact constraint matrix, $\mathbf{X}$ denotes the vector of contact nodes' initial coordinates and $\boldsymbol{\lambda}$ is the vector of Lagrange multipliers representing the contact force. Via explicit integration, the displacement is obtained as the sum of a trial solution without contact, $\mathbf{u}^*$, and a displacement increment due to contact forces, $\mathbf{u}^c$. The trial position vector $\mathbf{x}^*$ is derived from $\mathbf{u}^*$ and is used to check for penetration. In the FE model, the target surface is chosen as a function of the projected area of the impactor, slightly larger to properly define the contact, see Fig. 3.

The node-to-surface association is performed using a local contact search, while the exact contact point is obtained via the closest-point projection of the node onto the target surface [24, 25].

4 Numerical Results

In this section, three numerical cases are presented to evaluate the accuracy and efficiency of the 3D Hashin damage model for impact problems, combined with 2D CUF theories. The results are compared with the CODAM2 damage model [14], which implements 2D Hashin criteria, as well as with experimental results and ABAQUS analyses from the literature.

4.1 Elastic Impact

The spherical impactor, with a diameter of 16 mm, strikes a square composite plate with a side length of 100 mm, see Fig. 4. The composite plate is fully clamped along all four edges and impacted at its centre with an initial velocity of 5 m/s. The composite has a quasi-isotropic laminate with a stacking sequence $[90/45/0/\text{-}45]_{2s}$ and a total thickness of 2 mm. The material system is IM7/8552 CFRP, see Table 1.

The current analysis is linear-elastic, as the objective is to assess the stress field generated by the numerical model. The structural modelling of the composite plate adopts a set of 2D-CUF models, characterized by increasing orders of the Lagrange expansion through the thickness. In addition, a CUF model with three linear expansions per ply, referred to as CUF-3LE1/ply, is used. For verification purposes, the results are compared with a fully three-dimensional FE reference model from [13], which uses C3D8R solid elements with five elements through the thickness of each ply. Model details and degrees of freedom (DOF) are provided in Table 2.

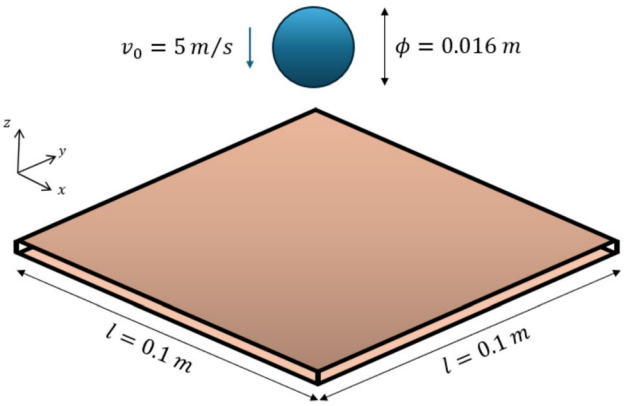


Fig. 4 Elastic impact of the square composite plate

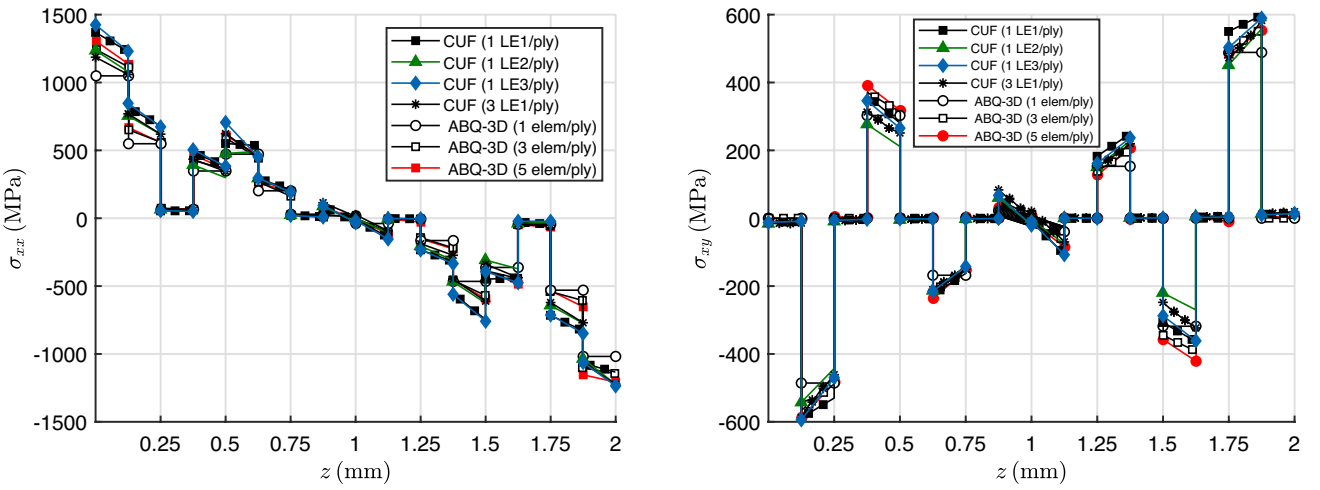
Table 2 Numerical models for the square plate. The ABAQUS models are from [13], ABQ-Refined is the one used as the benchmark

Model	Discretisation of the laminate	DOF
CUF-LE1	400 Q9 - 1 LE1/ply	85,731
CUF-LE2	400 Q9 - 1 LE2/ply	166,419
CUF-LE3	400 Q9 - 1 LE3/ply	247,107
CUF-3LE1	400 Q9 - 3 LE1/ply	247,107
ABQ-Refined	512,000 C3D8R - 5 el./ply	1,594,323
ABQ-Medium	307,200 C3D8R - 3 el./ply	964,467
ABQ-Coarse	102,400 C3D8R - 1 el./ply	334,611

Figures 5 and 6 show the through-thickness stress distributions near the center of the plate. Since the present assessment is restricted to the linear-elastic behaviour, the

Table 1 Elastic properties of IM7/8552 [13]

E_1 (GPa)	E_2 (GPa)	E_3 (GPa)	G_{12} (GPa)	G_{13} (GPa)	G_{23} (GPa)	ν_{12}	ν_{13}	ν_{23}	ρ (kg/m^3)
165.00	9.00	9.00	5.60	5.60	2.80	0.34	0.34	0.50	1700.00



(a) σ_{xx} (b) σ_{xy}

Fig. 5 In-plane stress components through the thickness of the composite plate under elastic impact at (x,y) = (48 mm, 48 mm)

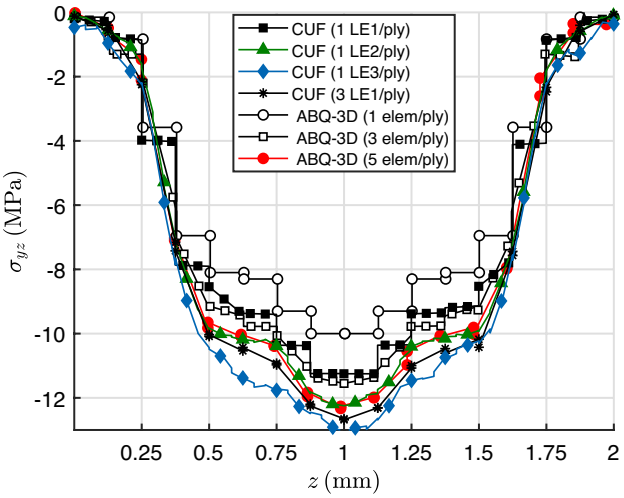


Fig. 6 Transverse shear stress through the thickness of the square plate under elastic impact at (x,y) = (40 mm, 40 mm)

through-thickness stress profiles are extracted at t=0.6 ms, corresponding to an early yet representative stage of the contact event, when the contact force is about $F \approx 2000\,\mathrm{N}$. A Hertz-type estimate [26] was adopted to assess the local normal stress scale beneath the impact point, i.e. at $(x, y) = (50, 50)\,\mathrm{mm}$. Assuming a rigid spherical impactor with radius $R = 8\,\mathrm{mm}$ and an equivalent elastic modulus E^* approximated as

$$E^* \approx \frac{E_3}{1-\nu_{23}^2} = \frac{9}{1-0.5^2}\,\mathrm{GPa} \approx 12\,\mathrm{GPa}, \tag{21}$$

the Hertz contact radius a_H is estimated as

$$a_H = \left(\frac{3FR}{4E^*}\right)^{1/3} \approx 1.0\,\mathrm{mm}. \tag{22}$$

This gives a peak Hertz pressure p_0

$$p_0 = \frac{3F}{2\pi a_H^2} \approx 0.95\,\mathrm{GPa}. \tag{23}$$

The computed local through-thickness normal stress beneath the impact point is $\sigma_{zz} \approx -0.96\,\mathrm{GPa}$, i.e. within about 1% of the Hertzian peak-pressure. Therefore, although the present node-to-surface formulation does not explicitly reproduce the analytical Hertz pressure distribution, it correctly captures the expected elastic contact stress. This is also consistent with previous studies, where the contact implementation within the CUF framework was validated against the analytical Hertz benchmark [27]. The deformed configuration is shown in Fig. 7.The results show that:

- There is a perfect match of in-plane stress fields for all models. As is well known, such stress components do not require refined models for high accuracy.
- Conversely, transverse stress fields have more demanding requirements. A single linear expansion (LE1) yields inaccurate results for the interlaminar shear stress σ_{yz}, which requires higher-order through-thickness expansions or multiple linear expansions per ply.
- The CUF-LE2 model is the lowest-order expansion that provides σ_{yz} similar to 3D FEM, but it requires only about 10% of DOF of the 3D model.
- Moreover, increasing the order of the through-thickness expansion leads to CUF results that progressively deviate from the ABAQUS predictions, see Fig. 6. This discrepancy is consistent with previous CUF papers [28], and shows how CUF enables a more effective refinement through the thickness and therefore reaches convergence faster than 3D FEM.

4.2 Circular Plate

The second numerical study considers the impact of a rigid sphere on a circular composite plate with a $[0/90]_{2s}$ stacking sequence and a ply thickness of 0.25 mm. The plate has a radius of 37.5 mm, a thickness of 2 mm, and is clamped at its lateral surfaces. The material is HTS40/9772 unidirectional CFRP. The impactor has a diameter of 15 mm, an initial velocity of 3.83 m/s, and a kinetic energy of 7.35 J. Material properties and cohesive parameters are in Tables 3 and 4. Seven cohesive elements are introduced through

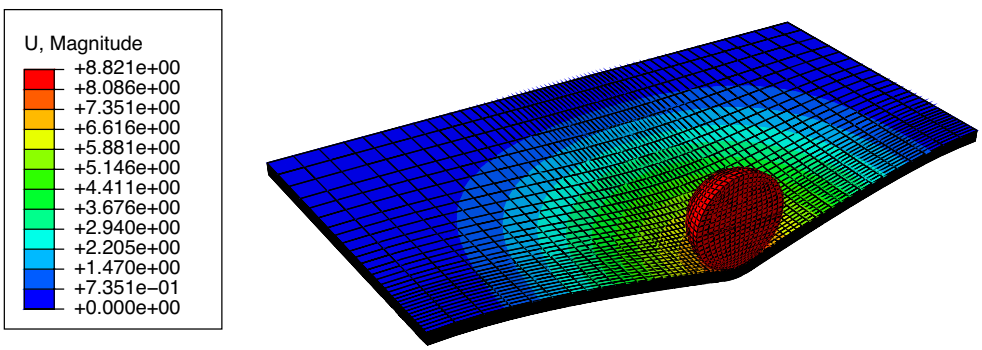


Fig. 7 3D deformation of the square plate under elastic impact

Table 3 Material properties of HTS40/9772 CFRP [13]

E_1(GPa)	E_2(GPa)	E_3(GPa)	G_{12}(GPa)	G_{13}(GPa)	G_{23}(GPa)	ν_{12}	ν_{13}	ν_{23}	ρ(kg/m^3)
153.0	10.3	10.3	6.0	6.0	3.7	0.3	0.3	0.4	1600.0
X_T(MPa)	X_C(MPa)	Y_T(MPa)	Y_C(MPa)	S_{12}(MPa)	S_{23}(MPa)	G_1^T(kJ/m^2)	G_2^T(kJ/m^2)	G_1^C(kJ/m^2)	G_2^C(kJ/m^2)
2537.0	1580.0	82.0	236.0	90.0	40.0	91.6	0.22	79.9	1.1

Table 4 Cohesive properties for the circular plate

Parameter	Mode I	Mode II	Mode III
Cohesive stiffness (GPa/mm)	137.33	49.33	49.33
Interlaminar strength (MPa) [13]	62.3	92.3	92.3
Interlaminar fracture toughness (kJ/m^2) [13]	0.28	0.79	0.79

Table 5 Numerical models for the circular plate

Model	Discretization of the laminate	DOF
132Q9/LE2	132 Q9 - 1 LE2/ply	39,816
192Q9/LE1	192 Q9 - 1 LE1/ply	38,448
192Q9/LE2	192 Q9 - 1 LE2/ply	57,672
192Q9/LE3	192 Q9 - 1 LE3/ply	76,896
260Q9/LE2	260 Q9 - 1 LE2/ply	77,832

the thickness, each with a thickness of 0.0075 mm, which is negligible compared to the total laminate thickness.

A mesh-convergence study of the peak impact force was performed using the CUF-LE2 expansion and varying in-plane discretizations with 132, 192, and 260 Q9 elements; see Fig. 8 and Table 5.

Figure 9 shows the effect of in-plane discretizations on the impact force curve, compared to experimental results [8]. The impact force-time curves were smoothed using MATLAB's function [29] with a centered moving-average filter and a 15% span. Based on the results of the mesh convergence study, the 192 Q9 mesh was chosen for subsequent analyses with different expansions. In particular, the results of linear (LE1), quadratic (LE2), and cubic (LE3) ply thickness expansion functions are shown in Fig. 10. In all cases, reference experimental [8] and numerical results [13] are provided for comparison. To quantify the effect of the structural theory on the agreement with the experiments, the Root Mean Square Error (RMSE) between the experimental and simulated force–time curves was computed, see Fig. 11. The RMSE is defined as

$$\mathrm{RMSE} = \sqrt{\frac{1}{N}\sum_{i=1}^{N}\left(F_{\mathrm{sim}}(t_i) - F_{\mathrm{exp}}(t_i)\right)^2}, \tag{24}$$

where $F_{\mathrm{sim}}(t_i)$ and $F_{\mathrm{exp}}(t_i)$ denote the simulated and experimental impact forces at the sampling instant t_i, respectively, and N is the number of samples. Figure 12

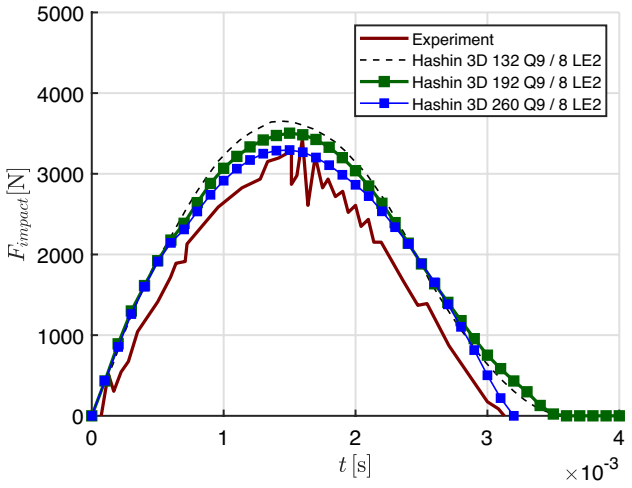


Fig. 9 In-plane mesh refinement effect of the impact force-time response for the circular composite plate with 15% smoothing. Experimental results are from [8]

shows the damage distribution at the maximum transverse displacement for the 192 Q9-LE3 model. Table 6 compares the predicted maximum values of intralaminar damage with the CODAM2 reference [13]. A further comparison is performed with the numerical and experimental results reported in [8]. The predicted distribution of matrix tensile damage in Fig. 13 shows good agreement with the numerical results presented in Fig. 10(a) of [8], where the matrix-damaged region extends to about 10 mm. Figure 14 shows the delamination shape computed by CUF, that is similar to

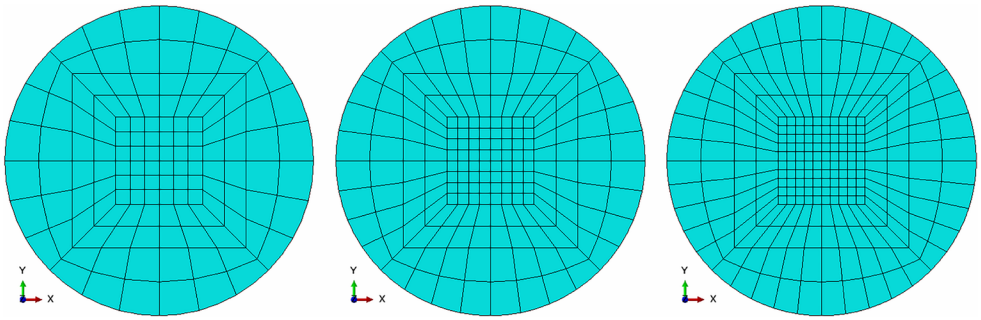
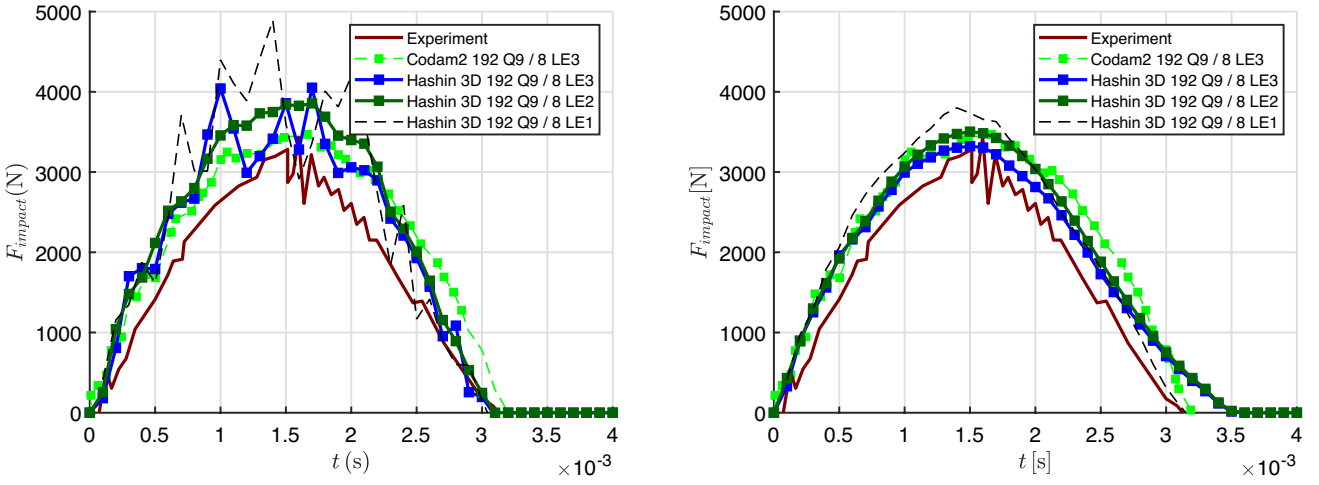


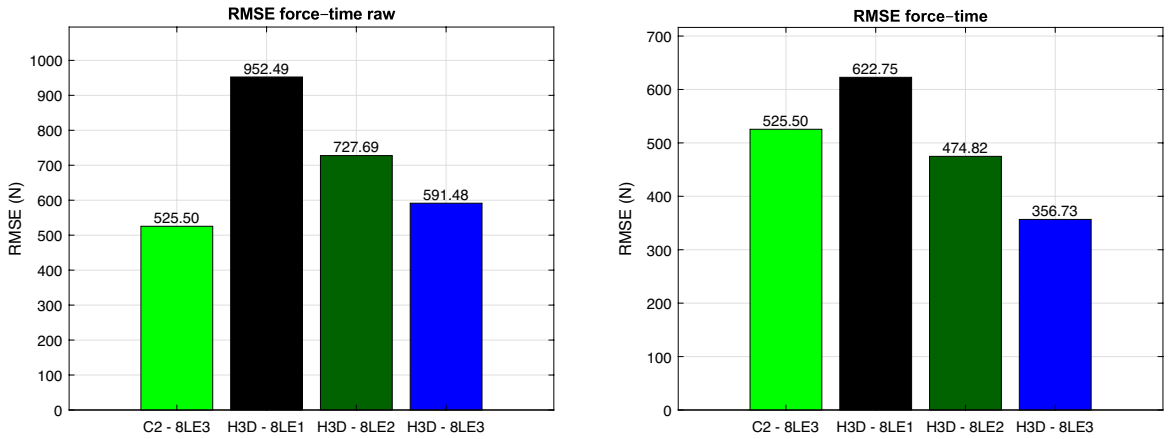
Fig. 8 132, 192, and 260 Q9 meshes used for the circular plate



(a) Raw curves.

(b) Curves 15% smoothed.

Fig. 10 Effect of through-thickness expansion order of the impact force-time response for the circular composite plate. Experimental results are from [8], CODAM2 reference results are from [13]



(a) RMSE computed between the simulated raw $F_{\text{sim}}(t_i)$ and experimental $F_{\text{exp}}(t_i)$ impact forces.

(b) RMSE computed between the simulated smoothed $F_{\text{sim}}(t_i)$ and experimental $F_{\text{exp}}(t_i)$ impact forces.

Fig. 11 RMSE of the force–time response for the circular plate. The CUF H–P approach is compared to RMSE values of CODAM2 from [13] (C2)

the numerical reference [8] in Fig. 8(a). Table 7 compares the estimated delaminated areas.

The results suggest that:

- Linear through-thickness expansions (LE1) overestimate the impact force and exhibit pronounced oscillations. As the order of the through-thickness expansion increases, the oscillations in the force–time response decrease. Overall, the application of smoothing effectively mitigates these oscillations, and increasing the order of the through-thickness expansion further improves the agreement with the experimental curve.
- For the 192 Q9-LE3 model, the damage contour maps indicate matrix-dominated progressive damage in both tension and compression, with only limited saturated fibre damage.
- Overall, the predicted damage state agree well with the numerical outcomes of Fig. 13 and 14 from [13]. The delamination area prediction is strongly affected by the in-plane element size in the impact region. In particular, reducing the element side length from 2.64 mm in the 192 Q9 mesh to 2.112 mm in the 260 Q9 mesh leads to a larger predicted delaminated area, from 17 mm^2 to 145 mm^2. This indicates that a finer in-plane discretization is required to properly activate and propagate cohesive damage. The latter value falls within the interval defined by the experimental estimate and the reference numerical delamination-evolution area,

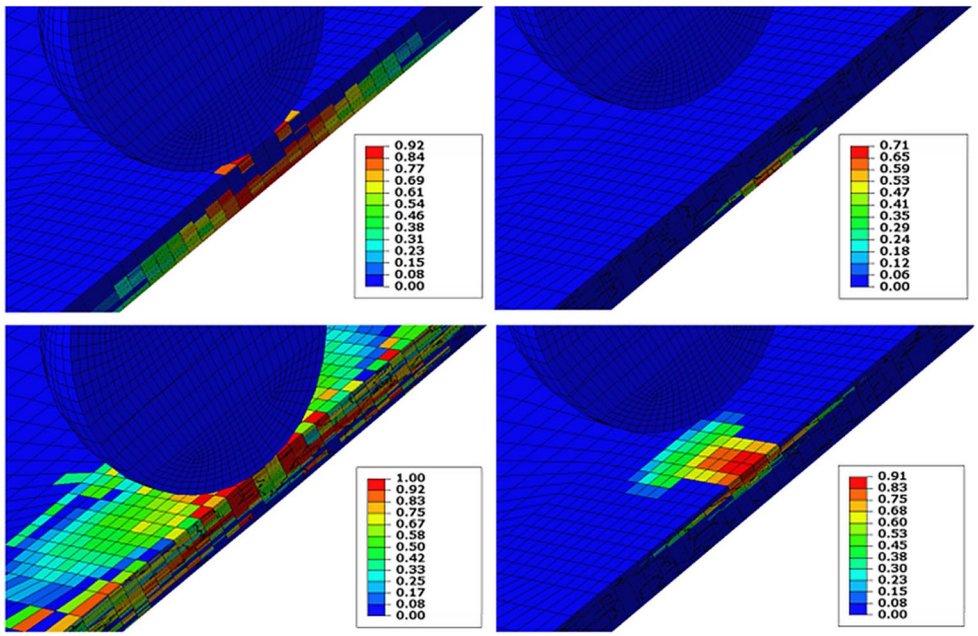


Fig. 12 Damage in the impact region of the circular plate, 192 Q9-LE3 model. Clockwise from the top-left: **a** Matrix tensile damage; **b** Fibre tensile damage; **c** Fibre compressive damage; **d** Matrix compressive damage

Table 6 Comparison of predicted maximum damage variables between CODAM2 and Hashin 3D

Damage mode	CODAM2 (d)	Hashin 3D (d)	Percentage difference
Matrix tensile damage	1.00	0.92	8.0%
Fibre tensile damage	0.86	0.71	17.4%
Fibre compressive damage	0.96	0.91	5.2%
Matrix compressive damage	1.00	1.00	0%

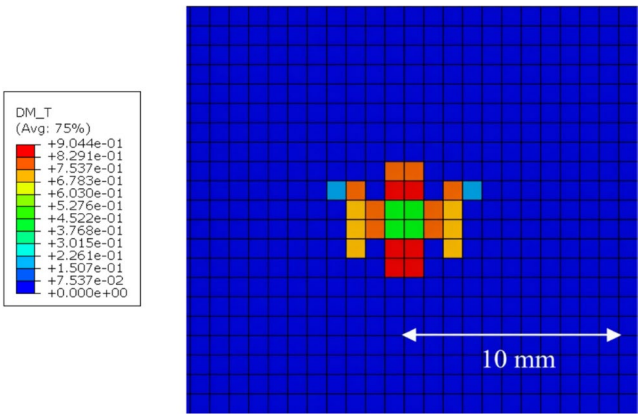


Fig. 13 Tensile matrix-damaged region in the upper surface of the circular plate, 192 Q9-LE3 model

Table 7 Comparison of estimated delaminated areas from experiments, reference numerical results [8], and present CUF predictions

Source	Estimated area (mm^2)
Experiment [8]	80.36
Reference numerical result [8, Table 4], complete failure ($d \geq 1$)	48
Reference numerical result [8], delamination evolution ($0 < d \leq 1$)	288
192 Q9-LE3 CUF, delamination evolution ($0 < d \leq 1$)	17
260 Q9-LE2 CUF, delamination evolution ($0 < d \leq 1$)	145

suggesting a more consistent prediction of the damage extension with the refined mesh.

- The present formulation captures back-face delamination, which was not predicted in [13]. The back-face delamination is experimentally confirmed at 14.7 J in [8], while it is not reported at 7.35 J. Therefore, its occurrence cannot be established from the available data; however, since delamination is already experimentally detected at this energy level, back-face damage remains a plausible component, likely less extensive than at 14.7 J.

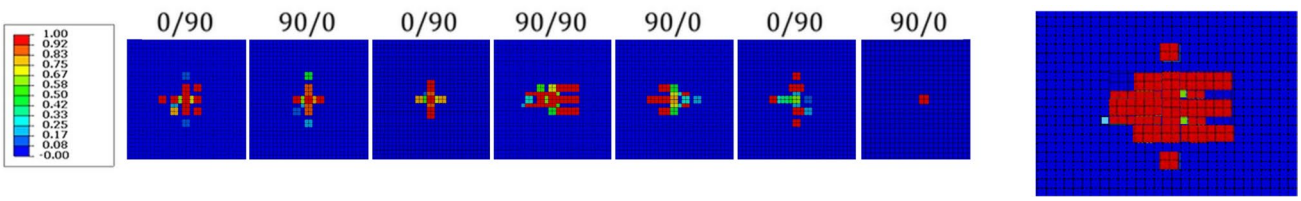


Fig. 14 Left: Delamination at the ply interfaces of the circular plate, ordered through the thickness from the impacted top surface to the bottom face. Right: Delamination envelope through the thickness, 260Q9-LE2 model

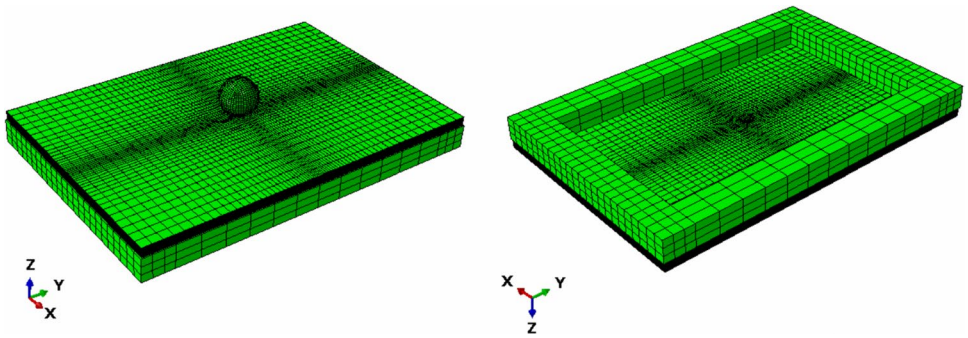


Fig. 15 Mesh adopted for the rectangular plate

Table 8 CUF model for the rectangular plate

DOF	Discretization
93,960	308 Q9 - 1 LE2/ply

4.3 Rectangular Plate

The last numerical case considers a three-body impact configuration comprising an impactor, a composite laminate, and a fixture base. The results are compared with the model for LVI damage in composite laminates reported in [7], which investigated several damage models and showed that linear damage evolution combined with cohesive elements provides a reliable and robust strategy for this class of simulations. The laminate has in-plane dimensions of 150 mm $\times$ 100 mm and a total thickness of 4 mm, with stacking sequence $[0/90/45/\text{-}45]_s$. The fixture base is rigid and fully constrained at the bottom, and it includes a central cutout measuring 125 mm $\times$ 75 mm, as shown in Fig. 15. The experimental setup is modeled as follows: the laminate specimen rests on the rigid base and is fully constrained on its upper surface over four circular regions of radius $r = 9.0$ mm, centered at $(x, y) = (9.38, 24.42)$, $(9.38, 125.58)$, $(90.63, 24.42)$ and $(90.63, 125.58)$. The impactor is a rigid sphere traveling at 5 m/s, with a 16 mm diameter and an impact energy of 25 J. Table 8 shows the CUF model information.

The material properties adopted in the present analyses are reported in Tables 9 and 10. Seven cohesive elements were introduced through the thickness, each with a thickness of 0.0075 mm.

Several guidelines have been proposed to select the penalty stiffness of cohesive elements [12]. Turon's penalty-stiffness guideline was used as a reference [30], and the penalty stiffnesses are set as:

Table 10 Cohesive properties for the rectangular plate

Parameter	Mode I	Mode II	Mode III
Cohesive stiffness (GPa/mm)	15.6	7.7	7.7
Interlaminar strength (MPa) [13]	60.0	90.0	90.0
Interface fracture energy (N/mm) [7]	0.6	2.1	2.1

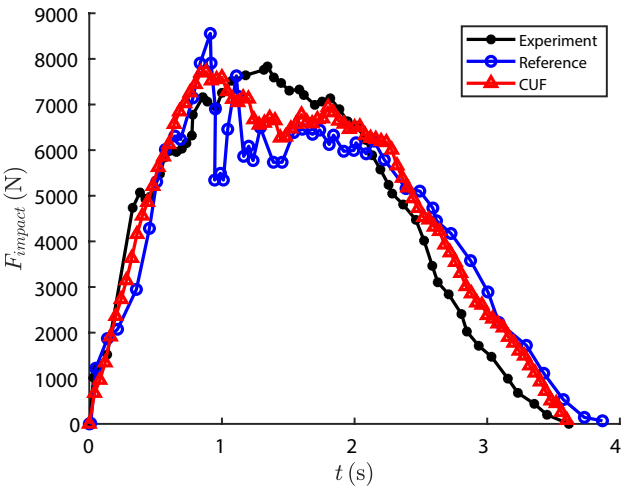


Fig. 16 Force–time response for the rectangular plate. CUF results with 8% smoothing

$$K_{\mathrm{I}} = \alpha \frac{E_3}{t_{\mathrm{ply}}}, \qquad K_{\mathrm{II}} = K_{\mathrm{III}} = \alpha \frac{G_{23}}{t_{\mathrm{ply}}}. \tag{25}$$

where K_I, K_{II}, and K_{III} are the cohesive penalty stiffnesses associated with Mode I - normal opening and Mode II/III - shear separations, respectively; E_3 is the through-thickness Young's modulus of a lamina; G_{23} is the transverse shear modulus; and t_{ply} is the ply thickness. Given the explicit time integration and the large-scale impact setting, $\alpha = 1$, verifying that this choice does not measurably affect the global elastic response. In the

Table 9 Material properties of T700GC/M21 [3, 4]

E_1 (GPa)	E_2 (GPa)	E_3 (GPa)	G_{12} (GPa)	G_{13} (GPa)	G_{23} (GPa)	ν_{12}	ν_{13}	ν_{23}	ρ (kg/m^3)
130.0	7.7	7.7	5.8	5.8	3.8	0.33	0.33	0.35	1600.0
X_T (MPa)	X_C (MPa)	Y_T (MPa)	Y_C (MPa)	S_{12} (MPa)	S_{23} (MPa)	G_1^T (kJ/m^2)	G_2^T (kJ/m^2)	G_1^C (kJ/m^2)	G_2^C (kJ/m^2)
2080.0	1250.0	60.0	140.0	110.0	110.0	133.0	0.6	40.0	2.1

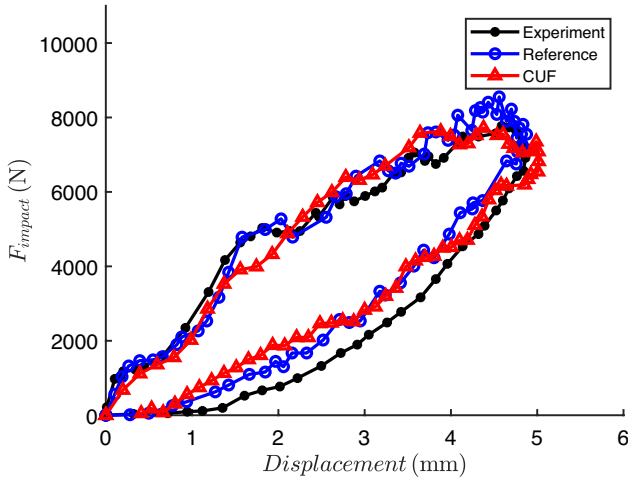


Fig. 17 Force-displacement curve for the rectangular plate. CUF results with 4% smoothing

Table 11 Peak force, F_{max}, and maximum displacement, u_{max}, for the rectangular plate. Experimental and reference values are obtained by graphical extraction

Model	u_{max}(mm)	F_{max}(N)	Δu_{max} vs Exp (%)	ΔF_{max} vs Exp (%)
Experiment [4]	4.59	7834	–	–
Reference [4]	4.54	8566	−1.09	+9.34
Simulation	4.36	7763	−5.01	−0.91

Table 12 Peak force, F_{max}, and peak time, t_{max}, for the rectangular plate. Experimental and reference values are obtained by graphical extraction

Model	t_{max}(ms)	F_{max}(N)	ΔF_{max} vs Exp (%)
Experiment [4]	1.34	7834	–
Reference [7]	0.91	8557	+9.23
Simulation	0.88	7763	−0.91

present case, the sublaminate thickness is assumed equal to the ply thickness, t_{ply} = 0.5 mm.

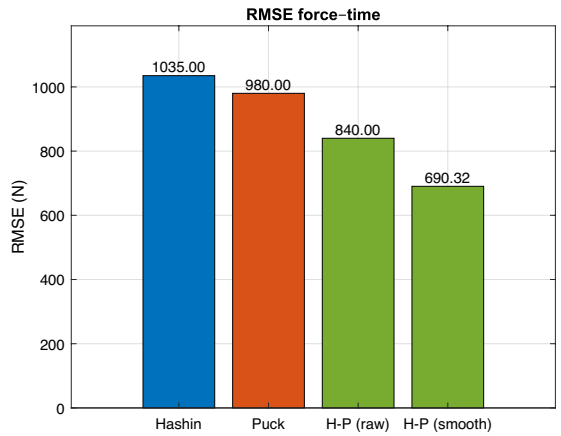
Figure 16 shows the impact force-time curves predicted by CUF, experiments [4], and the reference numerical results [7]. Figure 17 shows the force-displacement curve compared to the C2 case from [4]. The curves were smoothed using MATLAB's function [29] with a centred moving-average filter and an 8% maximum span.

Table 11 reports the peak impact force $F_{\max}$ and the maximum displacement $u_{\max}$, and the corresponding percentage deviations. It should be noted that the maximum impact force and the maximum displacement are not corresponding points, since they generally occur at different times during the impact event. Table 12 reports the time of peak forces.

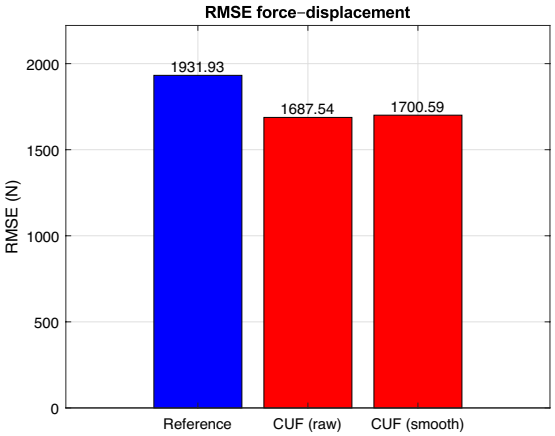
RMSE between the experimental and simulated force–time curves was computed for both the raw signal and the smoothed signal, as shown in Fig. 18a Moreover, an additional RMSE-based comparison of the force–displacement histories was also considered to assess the overall agreement with the experimental response, as shown in 18b

Figure 19 shows the evolution of the matrix damage, while Fig. 20 shows the delamination. Based on the experimental results for the C2 case reported in [4], delamination is caused by compressive fibre failure in the upper ply, the impacted face. As shown on the left-hand side of Fig. 21, the projected delaminated area exhibits an ogive-like shape, confirming the coupling between back-face delamination and upper-face compressive fibre damage, which is also captured by the present simulations.

The results show that:



(a) RMSE of the force–time response for the rectangular plate, computed between the simulated $F_{\text{sim}}(t_i)$ and experimental $F_{\text{exp}}(t_i)$ impact forces. The CUF H–P approach is compared to RMSE values of Hashin and Puck from [7].



(b) RMSE of the force–displacement response for the rectangular plate, computed between the simulated $F_{\text{sim}}(u_i)$ and experimental $F_{\text{exp}}(u_i)$ impact forces. The CUF approach is compared to reference value from [3].

Fig. 18 RMSE evaluation for the rectangular plate

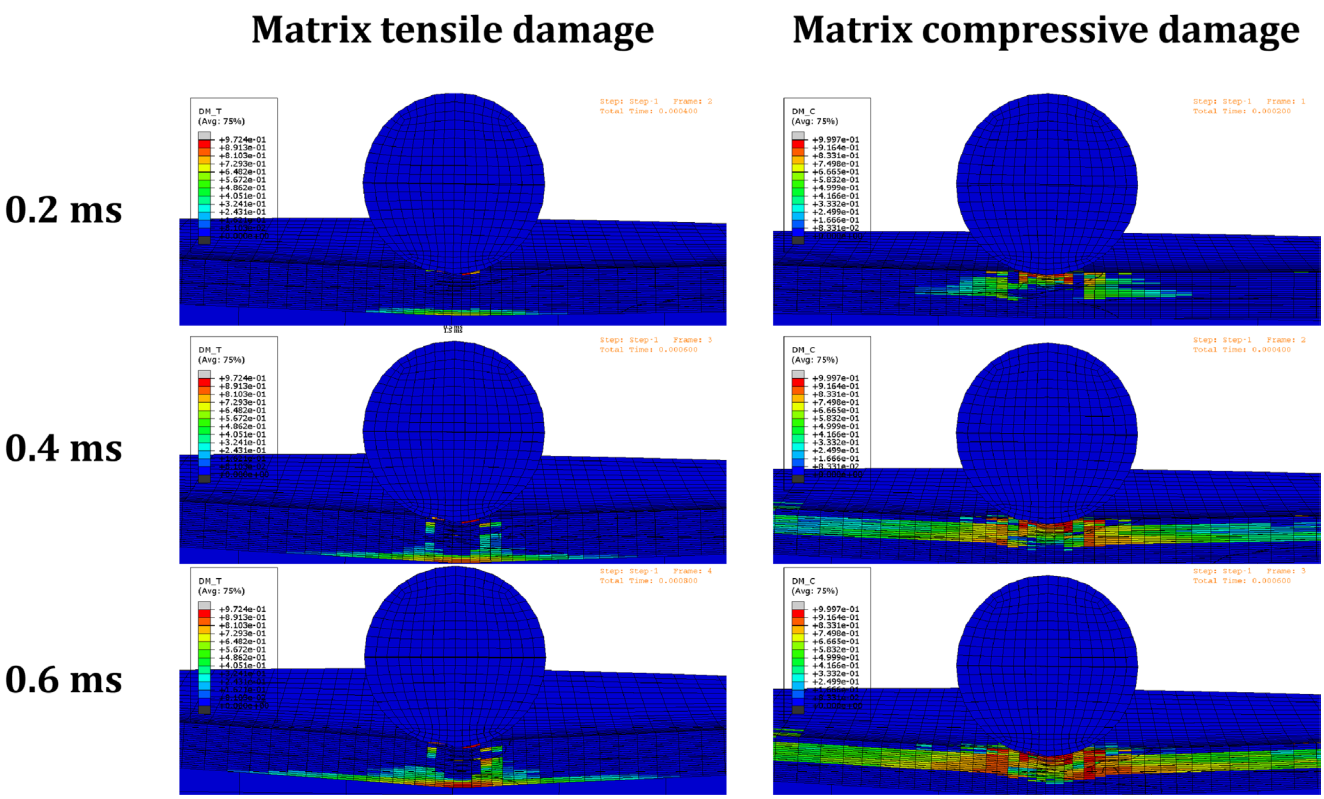


Fig. 19 Damage evolution in the matrix for the rectangular plate

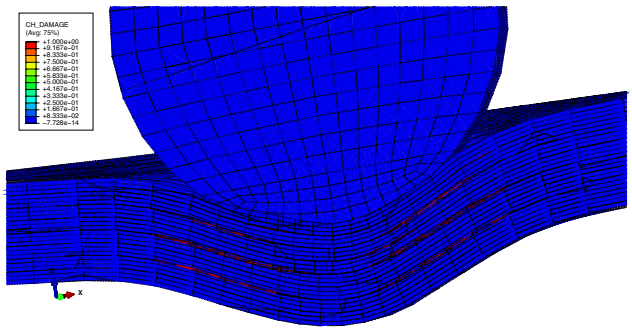
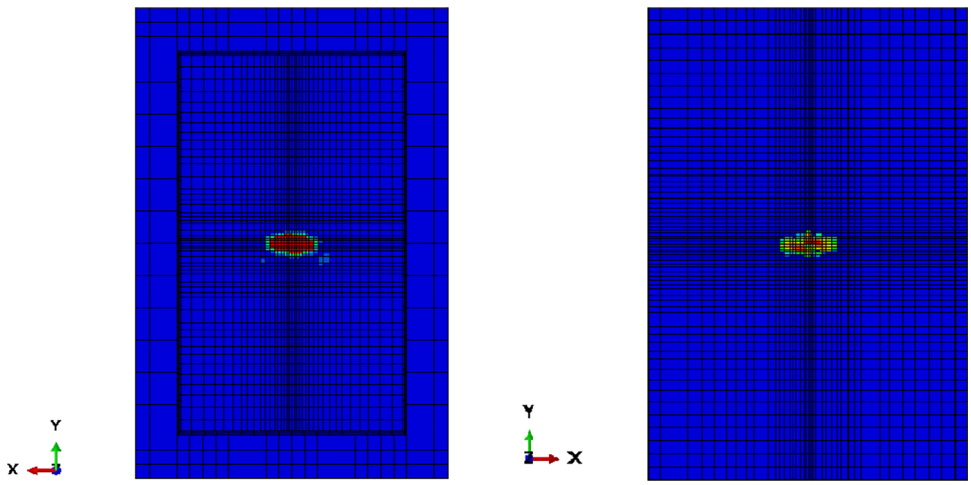


Fig. 20 Delamination at the impact point of the rectangular plate at t = 2.4 ms

- The use of a second-order expansion per element provides good accuracy compared to 3D FEM and experimental results.
- The present formulation reduces the oscillation behavior of the time-response.
- As seen in the previous section, comparisons with literature results confirm the proper detection of damage progression in-plane and through-the-thickness.

Fig. 21 Back-face delamination on the left and upper face fibre compressive damage on the right for the rectangular plate at t = 2.4 ms



5 Conclusions

This paper extends a layer-wise 2D-CUF impact framework to a 3D Hashin formulation, with mixed-mode cohesive elements to describe delamination. Preserving the efficiency of CUF models, this work improves the reliability of damage predictions in LVI scenarios by accounting for the full 3D stress state, including out-of-plane components. The approach's accuracy and computational efficiency have been assessed against numerical and experimental results from the literature and considering three numerical cases. The following main conclusions may be summarized:

- There is a consistent reduction of the computational costs across all the numerical cases. For instance, in the elastic case, a parabolic, layer-wise, displacement field over the thickness achieved stress predictions comparable to a 3D FE model while using 10 % of the 3D DOF.
- The extension and morphology of damage was successfully retrieved in all cases.
- Higher-order layer-wise kinematics alleviate the need for excessively refined in-plane meshes and through-the-thickness discretization.

Future work will focus on extending the present framework toward high-velocity impact (HVI) and more complex configurations like stiffened panels.

Acknowledgements This study was carried out within the Space It Up! project funded by the Italian Space Agency, ASI, and the Ministry of University and Research, MUR, under contract n. 2024- 5-E.0 - CUP n. I53D24000060005.

Author Contributions M.P. Conceptualization, revision M.F. Conceptualization, revision E.C. Conceptualization, revision C.F. Conceptualization, revision, writing and numerical analyses E.T. Conceptualization, revision

Funding Open access funding provided by Politecnico di Torino within the CRUI-CARE Agreement.

Data Availability No datasets were generated or analysed during the current study.

Declarations

Conflict of interest Marco Petrolo is serving as Editor-in-Chief for the journal and has not been involved in the peer-review process for this article in any way.

Open Access This article is licensed under a Creative Commons Attribution 4.0 International License, which permits use, sharing, adaptation, distribution and reproduction in any medium or format, as long as you give appropriate credit to the original author(s) and the source, provide a link to the Creative Commons licence, and indicate if changes were made. The images or other third party material in this article are included in the article's Creative Commons licence, unless indicated otherwise in a credit line to the material. If material is not included in the article's Creative Commons licence and your intended use is not permitted by statutory regulation or exceeds the permitted use, you will need to obtain permission directly from the copyright holder. To view a copy of this licence, visit http://creativecommons.org/licenses/by/4.0/.

References

1. Castanie, B., Azoti, W., Crouzeix, L., Bello, A., Taborda, R.P., Mahmood, A., Viste, A.: Review of monolithic composite laminate and stiffened structures in aeronautic applications. Composites Part C: Open Access **17**, 100585 (2025)
2. Kreculj, D., Boško, R.: Review of impact damages modelling in laminated composite aircraft structures. Tehnicki Vjesnik **20**, 485–495 (2013)
3. Liu, P.F., Liao, B.B., Jia, L.Y., Peng, X.Q.: Finite element analysis of dynamic progressive failure of carbon fiber composite laminates under low velocity impact. Compos. Struct. **149**, 408–422 (2016)
4. Hongkarnjanakul, N., Bouvet, C., Rivallant, S.: Validation of low velocity impact modelling on different stacking sequences of CFRP laminates and influence of fibre failure. Compos. Struct. **106**, 549–559 (2013)
5. Zhao, C., Fedulov, B.N., Liu, C., Zhang, K., Liu, H.: Establishment and development of an incremental constitutive model for CFRP considering the impact adiabatic effect. Aerotecnica Missili Spazio **105**(1), 49–62 (2026)
6. Rahman, M., Maravilla, E., Devaru, S., Lin, S. Waas, A., Ranatunga, V.: A computational method for predicting the damage and failure due to impact of double hat stiffened aircraft skin panels. *Aerotecnica Missili & Spazio*, 2026
7. Jin, Z., Zhou, Q., Wang, G., Pei, Z., Chen, G.: Robust generalized model for low-velocity impact damage in composite laminates. Polym. Compos. , (2025)
8. Shi, Y., Swait, T., Soutis, C.: Modelling damage evolution in composite laminates subjected to low velocity impact. Compos. Struct. 94(9), (2012)
9. Huang, K., de Boer, A., Akkerman, R.: Analytical modeling of impact resistance and damage tolerance of laminated composite plates. AIAA J. **46**, 2760–2772 (2008)
10. Xie, D., Salvi, A.G., Waas, A.M., Caliskan, A.: Discrete cohesive zone model to simulate static fracture in carbon fiber textile composites. In *Proc. 46th AIAA/ASME/ASCE/AHS/ASC Structures, Structural Dynamics and Materials Conf.*, Austin, April 2005. AIAA Paper 2005-2320
11. Williams, K.V., Vaziri, R., Poursartip, A.: A physically based continuum damage mechanics model for thin laminated composite structures. Int. J. Solids Struct. **40**(9), 2267–2300 (2003)
12. Song, K., Dávila, C.G., Rose, C.A.: Guidelines and parameter selection for the simulation of progressive delamination. In: Proceedings of the 2008 Abaqus Users' Conference, (2008)
13. Nagaraj, M.H., Carrera, E., Petrolo, M.: Progressive damage analysis of composite laminates subjected to low-velocity impact using 2D layer-wise structural models. Int. J. Non-Linear Mech. 127, (2020). (Art. no. 103591)
14. Nagaraj, M.H.: *Higher-order layer-wise models for the progressive damage and impact analysis of composite structures*. PhD thesis, Politecnico di Torino, 2021. Doctoral Dissertation, Doctoral Program in Mechanical Engineering (33rd Cycle), January 2021
15. Petrolo, M., Tortorelli, E., Saputo, S.: Compressive damage of composite structures using 3D Failure criteria and 2D

higher-order structural theories. *Mechanics of Advanced Materials and Structures*, pages 1–11, 2025
16. Petrolo, M., Tortorelli, E., Saputo, S., Carrera, E.: Tensile damage analysis of composite structures based on 3D Hashin failure criteria and 2D higher-order structural theories. Comp. Commun. **56**, 102395 (2025)
17" GrobidStyleApplied="Changed. Zhang, Y., Van Paepegem, W., De Corte, W.: An enhanced progressive damage model for laminated fiber-reinforced composites using the 3D Hashin failure criterion: a multi-level analysis and validation. Materials **17**(21),. (2024. Art. no. 7681)
18. Camanho, P.P., Dávila, C.G., de Moura, M.F.: Numerical simulation of mixed-mode progressive delamination in composite materials. J. Compos. Mater. **37**(16), 1415–1438 (2003)
19. Kaleel, I., Carrera, E., Petrolo, M.: Progressive delamination of laminated composites via 1D models. Compos. Struct. **235**, 111799 (2020)
20. Carrera, E., Cinefra, M., Petrolo, M., Zappino, E.: *Finite element analysis of structures through unified formulation*. John Wiley & Sons, 2014
21. Vaziri, R., Carrera, E., Petrolo, M., Nagaraj, M.H., Reiner, J.: Progressive damage analysis of composite structures using higher-order layer-wise elements. Compos. B Eng. **190**, 107921 (2020)
22. Liu, H., Tan, W., Gong, X., Zhang, C., Li, Y., Li, X., Ma, D.: Assessment of failure criteria and damage evolution methods for composite laminates under low-velocity impact. Comp. Struct. **207**, 727–739 (2019)
23. Carpenter, N., Taylor, R., Katona, M.: Lagrange constraints for transient finite element surface contact. Int. J. Numer. Meth. Eng. **32**(1), 103–128 (1991)
24. Hallquist, J., Goudreau, G., Benson, D.: Sliding interfaces with contact impact in large-scale lagrangian computations. Comput. Methods Appl. Mech. Eng. **51**(1–3), 107–137 (1985)
25. Benson, D., Hallquist, J.: A single surface contact algorithm for the post-buckling analysis of shell structures. Comput. Methods Appl. Mech. Eng. **78**(2), 141–163 (1990)
26. Hertz, H.: Über die berührung fester elastischer körper (On the contact of elastic solids). Journal für die Reine und Angewandte Mathematik **92**, 156–171 (1881)
27. Carrera, E., Petrolo, M., Nagaraj, M.H., Kaleel, I.: Contact analysis of laminated structures including transverse shear and stretching. Eur. J. Mech. A. Solids **80**, 103899 (2020)
28. Carrera, E., Elishakoff, I., Petrolo, M.: Who needs refined structural theories? Compos. Struct. **264**, 113671 (2021)
29. The MathWorks, Inc. `smooth` — smooth response data, 2026. Curve Fitting Toolbox documentation, 2026
30. Turon, A., Dávila, C.G., Camanho, P.P., Costa, J.: An engineering solution for mesh size effects in the simulation of delamination using cohesive zone models. Eng. Fract. Mech. **74**(10), 1665–1682 (2007)

Publisher's Note Springer Nature remains neutral with regard to jurisdictional claims in published maps and institutional affiliations.